ELSEVIER

Journal of Nuclear Materials 313–316 (2003) 1–10

journal of nuclear materials

www.elsevier.com/locate/jnucmat

Section 1. Reviews

Helical divertor operation and erosion/deposition at target surfaces in LHD

A. Sagara [a,*], S. Masuzaki [a], T. Morisaki [a], S. Morita [a], H. Funaba [a], M. Goto [a], Y. Nakamura [a], K. Nishimura [a], N. Noda [a], M. Shoji [a], H. Suzuki [a], A. Takayama [a], A. Komori [a], N. Ohyabu [a], O. Motojima [a], K. Morita [b], K. Ohya [c], J.P. Sharpe [d], LHD Experimental Group [a]

[a] National Institute for Fusion Science, 322-6 Orosi, Toki 509-5292, Japan
[b] Department of Nuclear Engineering, Nagoya University, Nagoya 464-8603, Japan
[c] Faculty of Engineering, The University of Tokushima, Tokushima 770-8506, Japan
[d] Idaho National Engineering and Environmental Laboratory, USA

Abstract

Divertor footprints have been identified within a few mm in accuracy after 10 000 shots. This is the large merit of the large helical device divertor for erosion/deposition studies due to high reproducibility with an external superconducting coils system. Helical distribution of divertor erosion is compared with the prediction from magnetic field characteristics. The measured net erosion depth is found to be about a factor 3 less than the estimated one. Numerical simulations have revealed the net erosion to be very sensitive to deposition of C impurity in the plasma. Eroded carbon atoms are mainly redeposited near the divertor tiles, and partly deposited near the divertor strike point, forming a mixed layer with promptly deposited metals. Deposited metals accumulate locally at the edge of microscale open pores and around grains of graphite. This kind of metals sink possibly plays an important role as an impurity source after the tiles installation. This aspect of 'microscopic-PSI study' is very informative for understanding macroscopic-PSI.

PACS: 52.40.Hf
Keywords: LHD; Divertor; Erosion; Deposition; Metal impurity; Graphite

---

1. Introduction

The large helical device (LHD) is the largest heliotron-type plasma machine with an external helical magnetic field system, which consist of continuously wound superconducting (SC) coils as seen in Fig. 1. Therefore the LHD has great advantages such as current-less steady operation, no dangerous current-disruption of plasma, and an intrinsic divertor configuration. The major goals of the LHD are (1) physics experiments from which break-even condition can be extrapolated ($nT\tau_E > 10^{20}$ keVm^{-3} s, $T > 10$ keV, $\beta > 5\%$), (2) demonstration of high performance steady-state operation of current-less plasma with a divertor [1–3].

After each experimental campaign in LHD, surface analyses of divertor targets are quite informative not only for engineering evaluation of net-erosion rates but also for characterization of the divertor flux distribution, and for a fundamental understanding of impurity and particle recycling mechanisms in high-density plasmas under high magnetic fields. These engineering and physical subjects are common and one of the top issues for fusion relevant plasma machines such as ITER [4]. For these PSI studies the LHD has many advantages,

---

[*] Corresponding author. Tel.: +81-572 58 2155; fax: +81-572 58 2618.
E-mail address: sagara@lhd.nifs.ac.jp (A. Sagara).

0022-3115/03/$ - see front matter © 2003 Elsevier Science B.V. All rights reserved.
PII: S0022-3115(02)01326-0

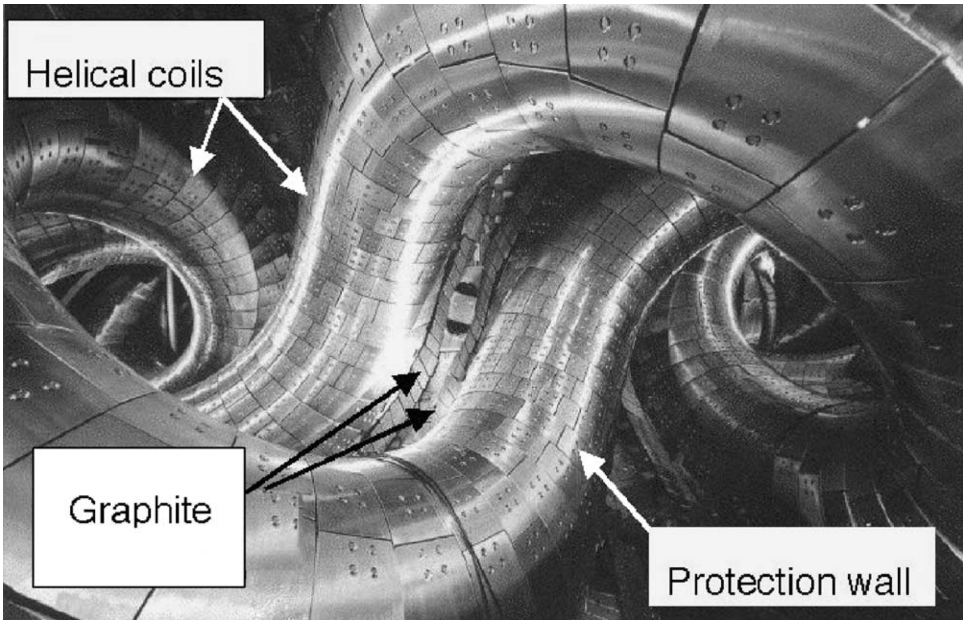

Fig. 1. A wide-angle photo looking at the inside of LHD, where the vacuum wall is covered with water-cooled stainless steel protectors and the divertor region between a pair of helical coils ($l = 2$, $m = 10$) is protected with graphite tile arrays. The major radius $R = 3.9$ m, minor plasma radius $\langle a_p \rangle = 0.6$ m, and $B_0 = 3$ T.

namely, a stable divertor structure formed by external SC coils, and high reproducibility of materials irradiation under operations at similar beta without plasma-current disruption.

In this paper the first results obtained from the divertor tiles used in LHD experiments are presented. Local erosion/deposition profiles and the macroscopic migration of materials are evaluated in comparison with numerical simulations [5], wall sample analyses [6] and collected dust analyses [7]. Microscopic morphology is found to be very important to understand impurity behavior. This new aspect is discussed by taking account of the historical change of impurity levels in the core plasma [8] and power radiation profiles [9] in the series of LHD campaigns.

2. Current status of LHD

The LHD experiment started in March 1998 after an 8-year construction period, and large progress has been made step by step in these five campaigns, such as in stored energy as typically shown in Fig. 2. From the third campaign graphite tiles were used for divertor targets. Heating power has increased up to 9 MW for NBI, 2.7 MW for ICRH and 1.8 MW of ECRH. The plasma parameters achieved in LHD are summarized in Table 1 [10].

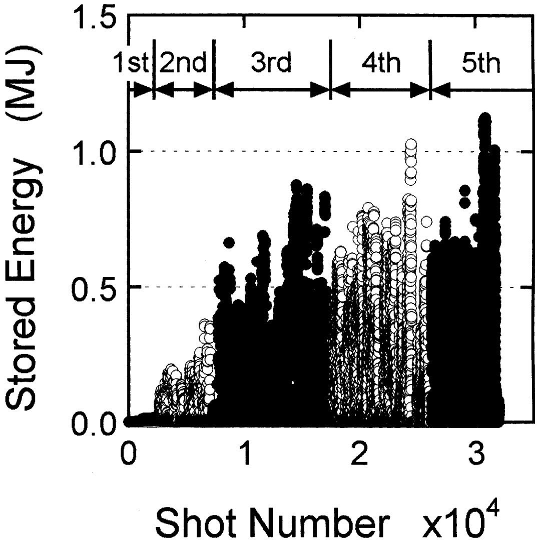

Fig. 2. Progress in plasma stored energy with the main discharge shots in LHD.

There have been many new findings and intensive studies on, for example, improvement of energy confinement by inward shift of the plasma axis [11], formation of an edge transport barrier [12], transition of radial electric field from negative (ion root) to positive

Table 1
Plasma parameters achieved in the fifth campaign (FY2001)

	Achieved parameters in LHD				
	T_e (keV)	T_i (keV)	τ_E (s)	P_{abs} (MW)	$\bar{n}_e$ (m^{-3})
Temperature	10	1.7	0.06	1.2	0.5×10^{19}
	3.6	5	0.14	4.1	0.7×10^{19}
Confinement	1.3	1.3	0.36	1.5	4.8×10^{19}
(Triple product)			($n_i \tau_E T_i = 2.2 \times 10^{19}$ keV m^{-3} s)		
Stored energy	1.16 MJ				
Beta	3.2% at 0.5 T				
Line-averaged deinsity	1.6×10^{20} m^{-3}				

(electron root) as predicted by neoclassical theory [13], characterization of divertor plasmas [14–17], long pulse discharge and impurity effects [18,19], particle balance [20], and so on. One of the recent highlights is the achieved $T_e(0)$ of more than 10 keV by highly focused 1.2 MW of ECH [21], where an internal transport barrier has been observed [22].

As for the next step, edge plasma control due to active pumping by installing a local island divertor [23], steady-state fueling of H_2 by pellet injection, and wall conditioning with wide area boronization using B_2H_6 are planned. Collaborative studies with universities and JAERI as well as international institutions have been encouraged and will be expanded more.

3. Characterization of helical divertor operation

From the third campaign in 1999, as shown in Fig. 1, the material for the divertor target was fully changed from stainless steel to 1742 pieces of graphite tiles (isotropic, IG-430U/Toyo Tanso Co.), which are mechanically joined (bolted) to water cooled copper plates [18]. In this work the divertor tiles used in the third campaign were selected for analysis, because the plasma operation conditions were very simple as described below. Fig. 3 shows the helical divertor arrangement, where two pairs of tile arrays are seen and the tiles analyzed in this work are indicated. Almost all tiles are arranged to be parallel at a glancing angle to the magnetic field line of divertor. A few tiles are at near normal incidence to the field lines as seen in Fig. 4, where the divertor plasma is clearly observed to strike the tiles placed inside the tangential port. Here we call the divertor plasma region a 'leg'.

The divertor plasma characteristics have been intensively investigated mainly using Langmuir probe (LP) arrays, which are set on several divertor tiles distributed in the helical direction, thermocouples embedded in divertor tiles, IR cameras for surface temperature, and a reciprocating-type fast scanning LP [15]. Profiles of core plasma parameters have been measured with YAG-laser Thomson scattering for electron temperature [24], a multi-chord far-infrared interferometer for density [25], and charge exchange recombination spectroscopy for ion temperature [13].

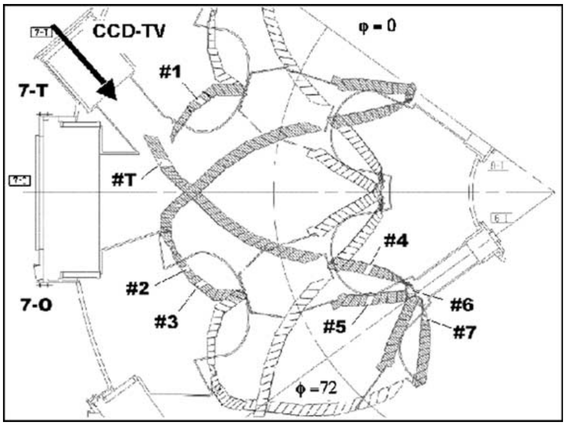

Fig. 3. The top view of one pitch (poloidally 360° and toroidally 72°) of double-null helical divertors, where two pairs of tile arrays are seen and the tiles (#1–7, #T) analyzed in this work are indicated. The CCD photo of Fig. 4 was taken at the 7-T port.

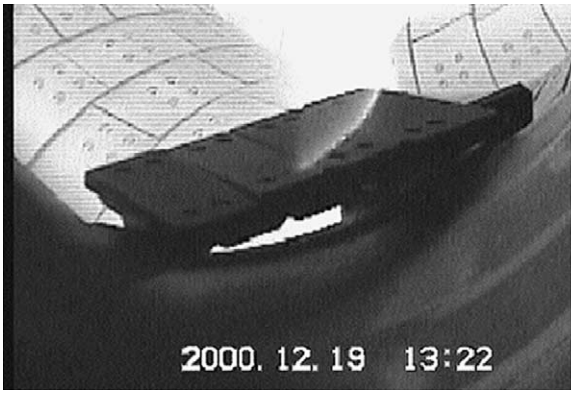

Fig. 4. A CCD photo taken with a Hα filter, where the divertor leg with a sharp width less than 10mm strikes the graphite tile placed in the tangential port 7-T as indicated in Fig. 3.

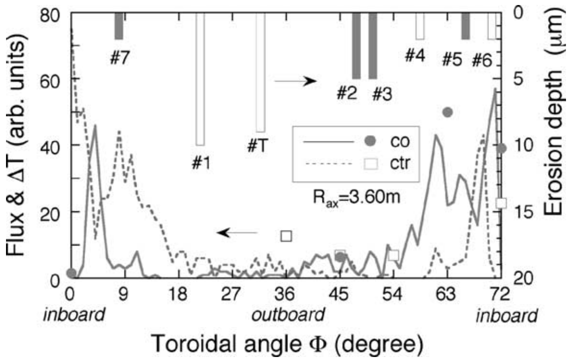

Fig. 5. Divertor flux (per unit tile) distributions (solid and dotted lines) calculated at $R_{ax} = 3.60$ m in comparison with heat flux measured by thermocouples (symbols), where 'co' means that the direction of particle flow is same as the magnetic field direction and 'ctr' is opposite. Erosion depth measured in this work is also indicated.

Fig. 5 shows the divertor flux distributions calculated by a field line tracing method coupled with the random walk process [17] for the case of the magnetic axis $R_{ax} = 3.60$ m. In this case the flux concentrates at the inboard side of the torus ($\phi = 0$ or 72° in Fig. 3), and good agreement is confirmed between calculations and the temperature rise measured with thermocouples. The erosion depth measured in this work is also indicated in Fig. 5, and will be discussed in Section 4.2. In the case of $R_{ax} = 3.75$ m, however, the flux concentrates at the up- and downside of the torus ($\phi = 18$ or 54°).

For erosion studies the evaluation of the particle flux, particle energy and exposure time is indispensable at the divertor tiles. It has been demonstrated that the particle flux Γ_{div} in front of the divertor tile increases simply with the line-averaged plasma density $\langle n_e \rangle$, while the electron temperature $T_{e,div}$ at the divertor tile is almost constant within the experimental range achieved so far in LHD [15]. Using the LP data measured at the outboard side divertor, the third campaign (shot # 7120–17 311) has been evaluated for all discharge shots, which include operations at different magnetic axes with the working gas of H_2, He or H_2 + He. Fig. 6 shows the Γ_{div} and $T_{e,div}$ measurements together with discharge duration time τ_d for the case of $R_{ax} = 3.60$ m. These results are used in Section 4.2.

After installation of graphite tiles, metal impurities markedly decreased. In fact the slow oscillation known as 'breathing' plasma, which is attributed in part to the influx of heavy impurities from sputtering of the stainless steel divertor [26], has clearly disappeared and a remarkable reduction of core radiation was observed

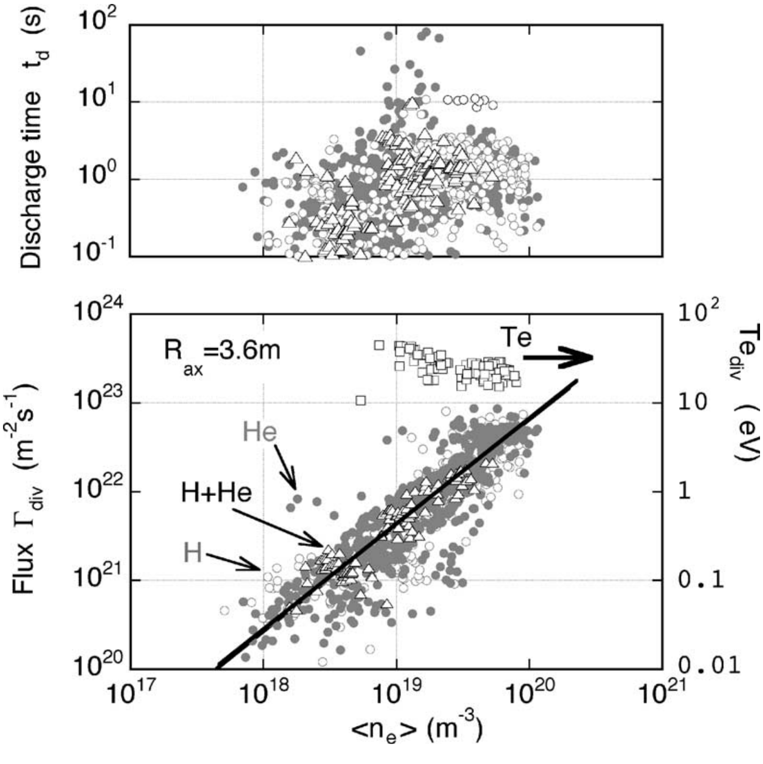

Fig. 6. Particle flux Γ_{div} and electron temperature $T_{e,div}$ measured at the outboard side divertor, and discharge duration time τ_d as a function of the line-averaged plasma density $\langle n_e \rangle$ in the third campaign.

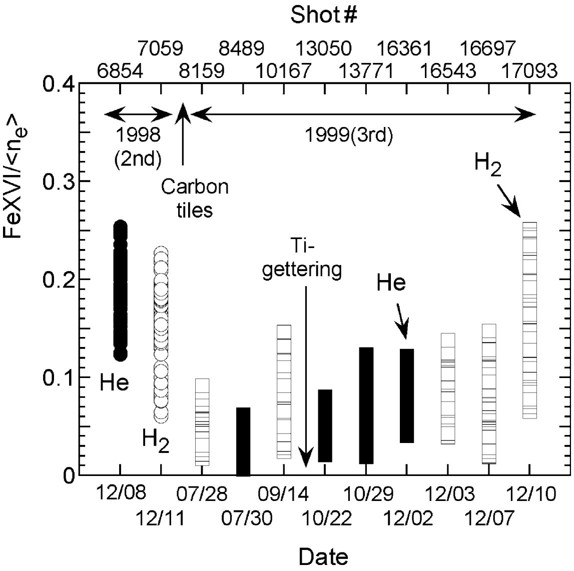

Fig. 7. FeXVI emission divided by electron density as a function of date (shot number). The data are taken at $R_{ax} = 3.6$ m with $B_0 = 2.75$–2.89 T ($P_{NBI} = 1.5$–2.0 MW) [8].

during NBI heated long pulse discharges [9], resulting in high-density operations up to $\langle n_e \rangle$ of 6×10^{19} m^{-3} [20]. VUV spectroscopy directly revealed the reduction of FeXVI as shown in Fig. 7 [8]. However, Fig. 7 also reveals that FeXVI gradually increases towards the same level as before the tile installation. The main reason might be attributed to the glow discharge cleaning (GDC) [27]. The details will be discussed in Section 4.3.

4. Erosion/deposition analyses

4.1. Identification of footprints

The fine structure of divertor legs at the target plates is known to have a complicated structure of magnetic field lines and it changes according to the vacuum magnetic configuration or the plasma beta value [16]. In fact many lines of ‘footprints’ are observed on the tiles used in the fourth campaign, for instance, as shown in Fig. 8. Therefore the first step is to identify the footprints within a few mm in accuracy. In this situation, as mentioned above, the tiles used in the third campaign were selected for analyses, because the experimental conditions for the magnetic configuration were fairly simple, that is, almost all shots were operated at the inward shifted R_{ax} of 3.60 m and only 17% were at the standard R_{ax} of 3.75 m.

For this purpose the tiles #2 and #T in Fig. 3 were selected, because the magnetic field line of the divertor leg intersects the #2 tile at a glancing angle of 64° from the normal (see Fig. 10). On the other hand, the angle of the field line on the #T tile is only 12° from the normal (see Fig. 9) and this condition is simple for comparison of experiments and modeling [28].

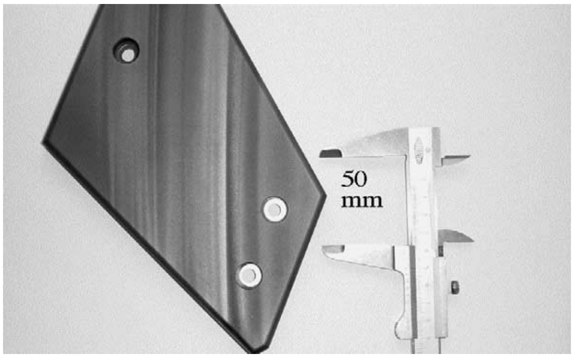

Fig. 8. A photo of the tile used in fourth campaign at the position #T indicated in Fig. 3 and seen in Fig. 4.

Figs. 9 and 10 show the results of impurity distribution and the erosion depth profile of the #T and #2 tiles, compared with the calculated connection length profiles L_c of the magnetic field lines, which correspond to particle flux profiles [16]. Metal impurities such as Fe were generally observed at about 3×10^{17} atoms/cm^2 on tiles. Here, on wall sample measurements using a shutter [6], it was confirmed that Fe deposition was clearly observed on the samples exposed to only GDC. On the sample exposed to only the main discharges, Fe deposition was not clearly observed. Therefore, including some amount of sputtered particles due to charge exchange neutrals during the main discharges, the main source may be attributed to deposition of sputtered metals from the stainless steel wall under GDC for a total of 2300 h with He or H_2. GDC is needed for wide area cleaning including NBI ports with the baking limited below 100 °C [27]. In this figure it is clear that the Fe and erosion profiles agree with the L_c profile at $R_{ax} = 3.6$ m. In the case of $R_{ax} = 3.7$ m, Fe contaminants are sputtered but the eroded depth is negligible. It is worth noticing that a small increase of Fe is observed at the opposite side of the private region. This will be discussed in the next section.

4.2. Erosion depth and numerical simulations

The toroidal angle dependence of erosion depth is summarized in Fig. 5. It is revealed that the depth on the outboard side tiles, namely #1, #T, #2 and #3, is deeper than the inboard side, namely #7, #4, #5 and #6. This result is opposite to the expectation from flux distributions in Fig. 5. One of the possible reasons might be a difference of the flux profile. In fact the LP measurements show a sharp profile at the outboard side but a broad profile at the inboard side in case of $R_{ax} = 3.6$ m [15]. Erosion can be confirmed with SEM photos as

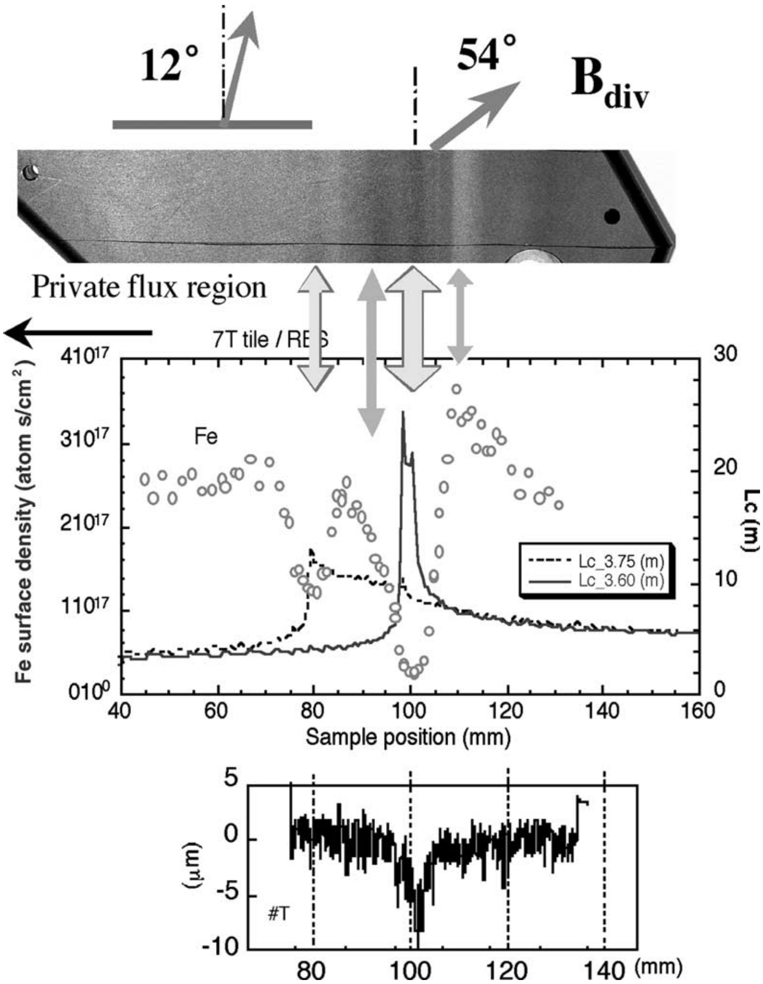

Fig. 9. Fe distribution measured by RBS on the #T tile surface, profiles of magnetic field connection length L_c in the cases of $R_{ax} = 3.6$ and 3.75 m, the erosion profile measured by surface profilometry, and the surface photo of footprints with an indication of the magnetic field direction.

shown in Fig. 11, where a 'smoothed shape' and 'spoon cut' shape are typically observed for the cases of glancing and near normal incidence of the field lines, respectively.

Using the LP data in Fig. 6, the total erosion depth expected after the third campaign was estimated by summing up $Y_s \Gamma_{div} \tau_d / n_c$ of each shot, where we used the sputtering yield $Y_s = 0.05$ for C by He at the impact energy 200 eV ($2T_i + 3qT_e$, approximating $T_e = T_i$ with a typical value of about 24 eV) and 0.002 for H at 100 eV [29], the curve fitted formula $\Gamma_{div} = 0.092\langle n_e \rangle^{1.1924}$, discharge duration time τ_d, and carbon density $n_c = 1.5$ g/cm^3. The result is shown in Fig. 12. The total fluence and discharge time for He are 2×10^{25} m^{-2} and 1983 s, and those for H are 1.2×10^{25} m^{-2} and 927 s in the case of $R_{ax} = 3.6$ m.

Numerical simulations of erosion profiles for the same condition described above have been performed using the three dimensional code EDDY based on a binary collision model in solids and the transport model in a magnetized plasma, which includes the Lorentz motion with friction forces and the atomic processes of ionization [5]. In this work the code has been modified to simulate a glancing thin plasma layer such as in the LHD divertor leg. Under the condition of $n_e = 1 \times 10^{18}$ m^{-2}, $T_e = 24$ eV and $B_{div} = 1$ T, the typical result for the #2 tile is shown in Fig. 13. Here, the concentration of impurities relative to the plasma density was typically assumed to be 2% of C ($\Delta Z_{eff} = 0.6$), <1% of O ($\Delta Z_{eff} < 0.6$) and 0.1% of Fe ($\Delta Z_{eff} = 0.4$) roughly estimated from the measured $Z_{eff} = 2.5$ in the third campaign [8]. In this figure the result means that the He

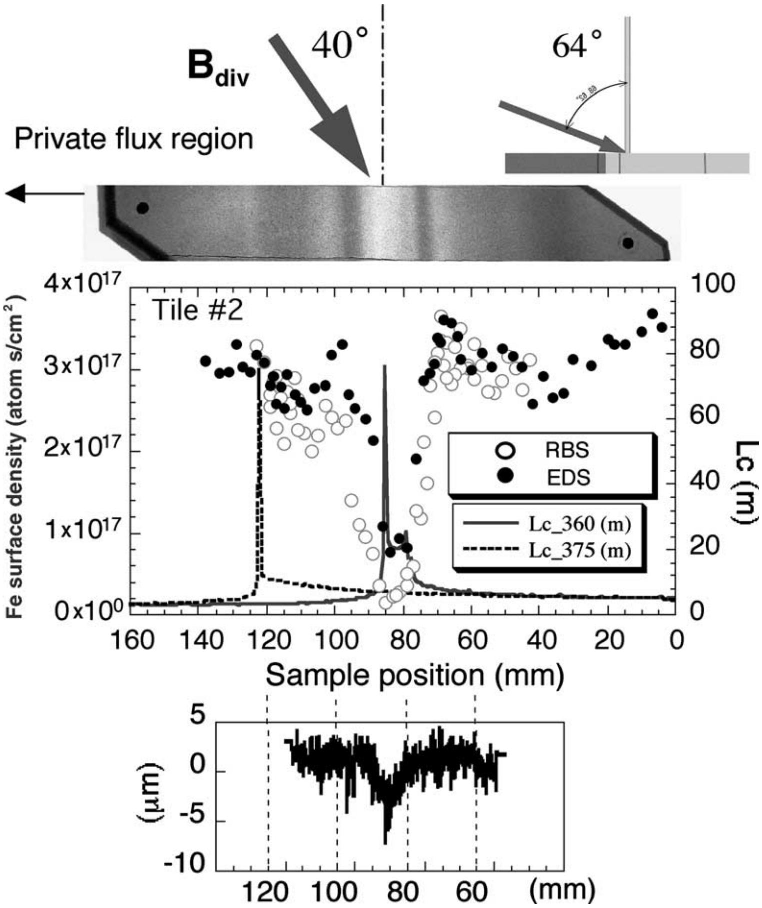

Fig. 10. Fe distribution measured by RBS and EDS on the #2 tile surface, profiles of magnetic field connection length L_c in the cases of $R_{ax} = 3.6$ and 3.75 m, the erosion profile measured by surface profilometry, and the surface photo of footprints with an indication of the magnetic field direction.

plasma causes a net erosion but the H plasma causes a net deposition of C impurity within the present condition. This is easy to understand, because the impurity concentration in the plasma was comparable to the sputtering yield of H. The total net erosion depth, therefore, is about 5 μm, which agrees very well with the measured depth as shown in Fig. 12. The overall particle balance of C should be investigated consistently by taking the toroidal/poloidal dependence into account, but this work will be left to the future. The simulation also reveals an asymmetric accumulation of Fe due to redeposition with vxB, where C does not show prompt redeposition due to its light mass [30]. Since the ionization lengths of sputtered C atoms are on the order of cm in this condition, they are assumed to deposit near the diverter area. In fact, according to the wall sample analyses, C deposition was mainly on the wall near the divertor legs [6].

4.3. Microscopic distribution of impurities

Fig. 14 shows the Fe distributions in EDS with SEM photos comparing typical positions for the eroded area, redeposited area and outside of the divertor leg on the #2 tile, namely at 80, 70 and 140 mm in Fig. 10, respectively. At the outside area of the divetor leg, the Fe impurity mainly due to GDC is uniformly distributed as a C mixed material with a thickness of about 100 nm, according to RBS analyses as shown in Fig. 15. On the other hand the Fe distribution inside the divertor strike area is not uniform. In the eroded area the major part of tile surface is pure carbon, in other words, metal impurities accumulate locally at the edge of open pores and around grains of graphite, even in the eroded area. RBS analyses revealed that these metals are distributed deeper than 1 μm. Those metals are assumed to be one of the main reasons why the metal impurity gradually

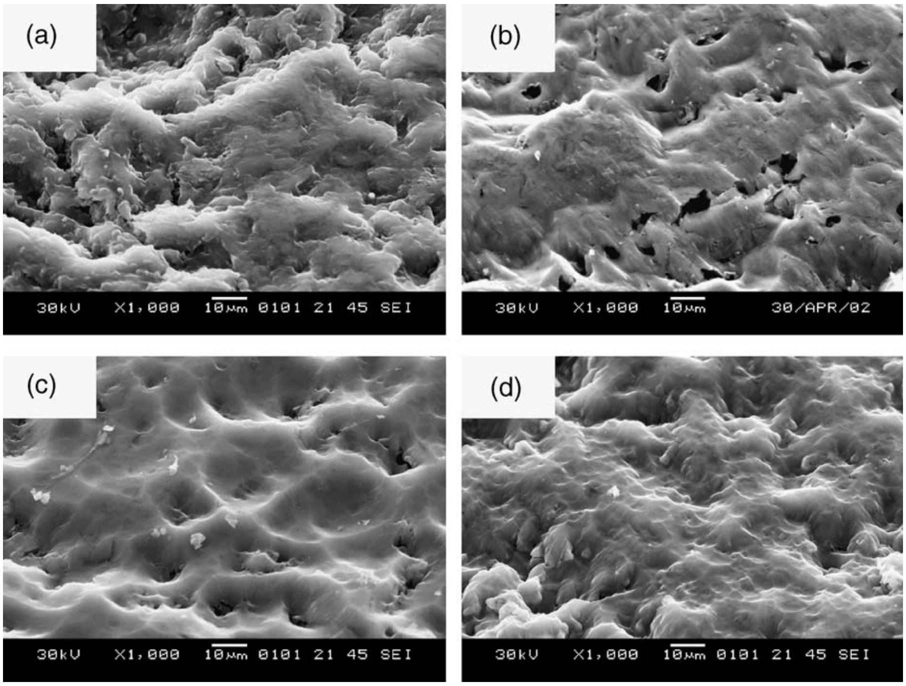

Fig. 11. SEM photos of (a) the original surface, (b) the eroded area ($x = 85$ mm) in Fig. 10, (c) the eroded area ($x = 100$ mm) in Fig. 9, (d) the Fe peaked area ($x = 110$ mm) in Fig. 9.

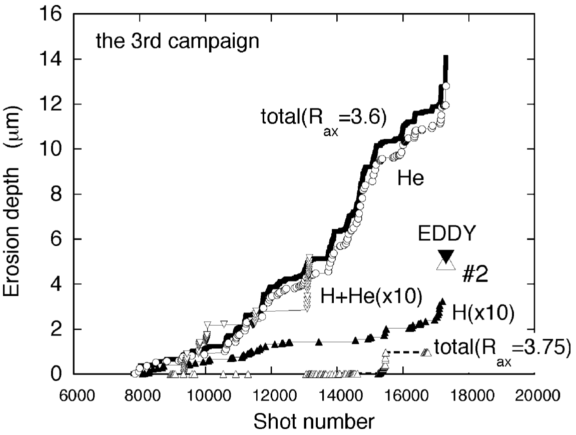

Fig. 12. Erosion depth estimated using the measured data of Fig. 6, measured depth on the tile #2 and the result of the numerical simulation with EDDY.

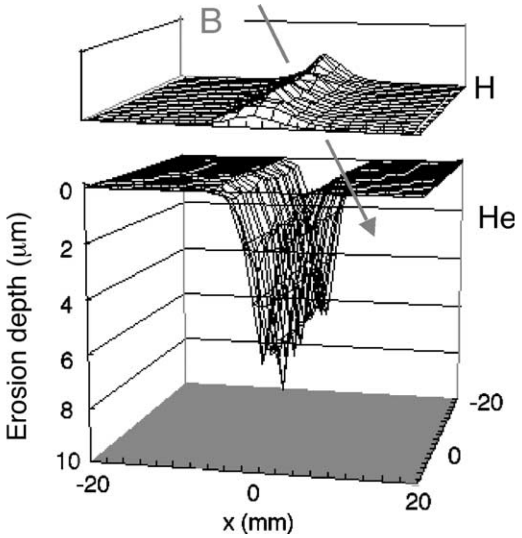

Fig. 13. Numerical simulations using EDDY of the net erosion of carbon under the same plasma condition for the tile #2.

increased towards the same level as before the tile installation as shown in Fig. 7. Wide area boronization is planned for the next campaign, and we can expect a reduction of metal impurities.

Redeposition is important not only due to safety issues but also from the impurity point of view for extended machine operation. Redeposition areas besides the erosion area are covered with mixed materials, which may not have the same property as the base material. Therefore, when operation conditions are changed and divertor legs strike these redeposition materials, there may be some kind of thermal stress, deforming the redeposited layers and then giving rise to dust formation.

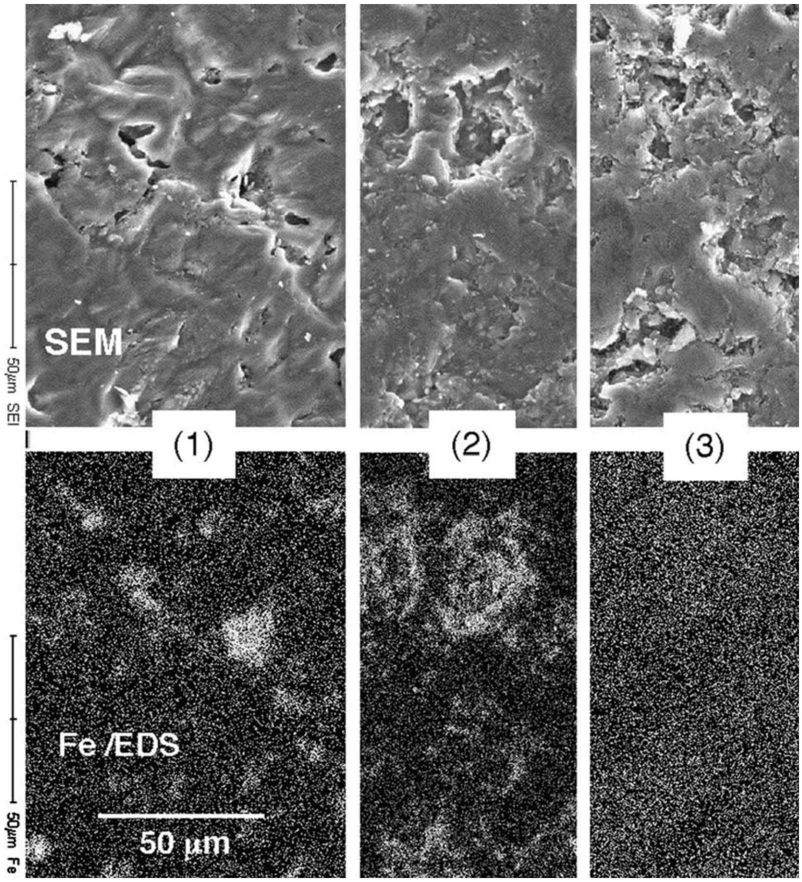

Fig. 14. Fe distributions in EDS (lower) with SEM photos (upper) comparing (1) the eroded area, (2) redeposited area and (3) outside of the divertor leg on the #2 tile, namely at 80, 70 and 140 mm in Fig. 10, respectively.

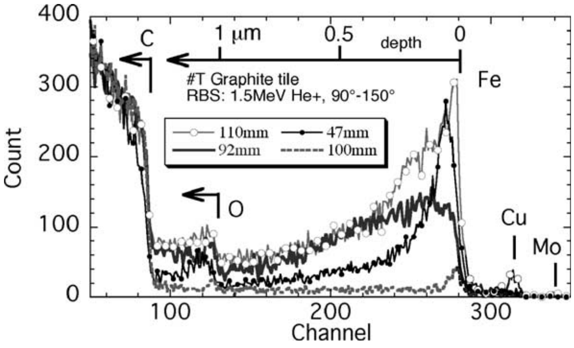

Fig. 15. RBS spectra measured on #T tile at each position described in Fig. 9. These spectra represent atomic depth profiles for each element.

In LHD dust collection and analysis have been performed just after the fourth campaign, resulting in a small amount of dust consisting of Fe–C mixed materials [7]. The behavior of the redeposited materials near the divertor legs is one of the important issues for future studies.

5. Conclusion

There has been large progress in these five campaigns in LHD, and it has been made clear by the installation of graphite tiles for the divertor target that plasma-wall interactions dominate at the divertor strike points.

Divertor footprints have been identified within a few mm in accuracy after 10 000 shots. This is a large merit of the LHD divertor for erosion/deposition studies due to high reproducibility with external SC coils system under operations at similar plasma beta. Due to this advantage, the helical distribution of the divertor erosion has been correlated successfully with predictions from magnetic field characteristics.

The measured net erosion depth is found to be about a factor 3 less than the estimated one. Numerical simulations have revealed the net erosion to be very sensitive to the deposition of C impurity in the plasma, because the sputtering yield is comparable to the impurity concentration.

Eroded carbon atoms are mainly redeposited near the divertor tiles, and partly deposited near the divertor strike point, forming a mixed layer with promptly deposited metals. The behavior of these redeposited layers is one of the important issues for extending machine operations.

In particular the deposited metals accumulate locally at the edge of open pores and around grains of graphite. This kind of metals sink may play an important role as an impurity source after the tile installation. Therefore this aspect of 'microscopic-PSI study' is very important for understanding macroscopic-PSI.

References

[1] A. Iiyoshi et al., Nucl. Fusion 39 (1999) 1245.
[2] M. Fujiwara et al., Nucl. Fusion 39 (1999) 1659.
[3] O. Motojima et al., Phys. Plasma 6 (1999) 1843.
[4] G. Federici et al., Nucl. Fusion 41 (2001) 1967.
[5] K. Ohya et al., J. Nucl. Mater. 258–263 (1998) 1055.
[6] T. Hino et al., in these Proceedings. PII: S0022-3115(02)01415-0.
[7] J.P. Sharpe et al., in these Proceedings. PII: S0022-3115(02)01360-0.
[8] S. Morita et al., Phys. Scrip. T 91 (2001) 48.
[9] B.J. Peterson et al., J. Nucl. Mater. 290–293 (2001) 930.
[10] A. Komori et al., Phys. Plasma 8 (2001) 2002.
[11] H. Yamada et al., Phys. Rev. Lett. 84 (2000) 1216.
[12] N. Ohyabu et al., Phys. Rev. Lett. 84 (2000) 103.
[13] K. Ida et al., Phys. Rev. Lett. 86 (2001) 5297.
[14] S. Masuzaki et al., J. Nucl. Mater. 290–293 (2001) 12.
[15] S. Masuzaki et al., Nucl. Fusion 42 (2002) 750.
[16] T. Morisaki et al., Contrib. Plasma Phys. 40 (2000) 266.
[17] T. Morisaki et al., Contrib. Plasma Phys. 42 (2002) 321.
[18] N. Noda et al., Nucl. Fusion 41 (2001) 779.
[19] Y. Takeiri et al., Plasma Phys. Control. Fusion 42 (2000) 147.
[20] Y. Nakamura et al., J. Nucl. Mater. 290–293 (2001) 1040.
[21] S. Kubo et al., J. Plasma Fusion Res. 78 (2002) 99.
[22] T. Shimozuma et al., in: Proc. 12th Joint Workshop on Electron Cyclotron Emission and Electron Cyclotron Resonance Heating, Aix-en-Provance, France, 2002.
[23] A. Komori et al., in these Proceedings. PII: S0022-3115(02)01491-5.
[24] K. Narihara et al., in: Proc. 18th IAEA Conference, Sorrent, 2000, EXP5/28.
[25] K. Tanaka et al., Rev. Sci. Instrum. 72 (2001) 1089.
[26] B.J. Peterson et al., Nucl. Fusion 41 (2001) 519.
[27] A. Sagara et al., J. Plasma Fusion Res. 75 (1999) 263.
[28] A. Sagara et al., J. Nucl. Mater. 196&198 (1992) 271.
[29] N. Matsunami et al., IPPJ-AM-14, Nagoya University, 1980.
[30] K. Ohya, A. Sagara, J. Plasma Fusion Res. 78 (2002) 840.